Research Square

Preprints are preliminary reports that have not undergone peer review.
They should not be considered conclusive, used to inform clinical practice,
or referenced by the media as validated information.

A 160°×160°Dynamic Holographic Meta-Projector

Zi-Lan Deng

zilandeng@jnu.edu.cn

Jinan University https://orcid.org/0000-0003-3861-6014

Feng-Jun Li

Jinan University

Rui-Xing Xia

University of Science and Technology of China

Qian-Mei Deng

Jinan University

Yu-Ze Lu

University of Science and Technology of China

Xiangping Li

Jinan University https://orcid.org/0000-0003-0955-2613

Fang-Wen Sun

University of Science and Technology of China https://orcid.org/0000-0002-9625-7390

Dong Zhao

University of Science and Technology of China https://orcid.org/0000-0001-7173-0500

Kun Huang

University of Science and Technology of China https://orcid.org/0000-0002-9391-149X

Article

Keywords:

Posted Date: February 13th, 2026

DOI: https://doi.org/10.21203/rs.3.rs-8421937/v1

License: This work is licensed under a Creative Commons Attribution 4.0 International License.
Read Full License

Additional Declarations: There is **NO** Competing Interest.

Abstract

Achieving real-time, reconfigurable wavefront control with dynamic metasurfaces remains a key unsolved challenge in photonics, fundamentally limiting their use in adaptive imaging and holographic displays. Conventional liquid-crystal spatial light modulators (SLMs) enable dynamic photonics but suffer from narrow fields of view (FOV) due to their micron-scale pixel pitch, constraining immersive three-dimensional visualization. Here, we present a pixel-interpolation-assisted holographic meta-projector that merges the dynamic tunability of SLMs with the subwavelength precision of metasurfaces. By integrating multiple metasurface nano-pixels within each SLM pixel and implementing a smart k-space distortion correction strategy for ultra-wide angles, the system achieves high-fidelity, real-time holographic video reconstruction with a FOV of 160°×160°—the widest ever demonstrated for dynamic holography—at 60 Hz refresh rate. This system represents the state-of-the-art near-full-screen holographic dynamic display, establishing a scalable pathway toward wide-FOV, high-speed virtual/augmented reality and adaptive optical systems.

Introduction

The realization of truly dynamic metasurface wavefront shaping remains one of the most fundamental and unresolved challenges in modern nanophotonics. Although reconfigurable metasurfaces have been heralded as the next frontier of flat optics—offering, in principle, arbitrary and ultrafast control of light at subwavelength scales—their practical implementation has been hindered by the absence of an effective mechanism for continuous, high-speed modulation and large field-of-view (FOV) of optical responses in nanostructured media. Existing metasurfaces, composed of static subwavelength resonators, achieve exquisite control over amplitude, phase, and polarization, but their optical functions are essentially “frozen” after fabrication. Attempts to endow them with dynamic tunability—through mechanical stretching[1], refractive-index modulation in tunable media[2–5], cavity deformation[6,7], or phase-change materials[8,9]—have yielded only discrete and often sluggish modulation states. Consequently, genuine dynamic metasurface wavefront control—a prerequisite for real-time light-field shaping—has not yet been realized, severely constraining the translation of metasurface research into dynamic display and holography applications.

In contrast, liquid-crystal spatial light modulators (SLMs)[10–14] have long provided a reliable route to dynamic light-field modulation. However, their micrometer-scale pixel pitch fundamentally limits the achievable diffraction angle[15], yielding a narrow FOV[16–18] that falls far short of the demands of emerging immersive display technologies such as augmented and virtual reality. Further pixel miniaturization in liquid-crystal SLMs is impeded by inter-pixel crosstalk, arising when pixel dimensions approach the transitional scale of liquid-crystal molecules[19,20]. As a result, even the most advanced SLM-based holographic displays remain confined to modest FOVs at the level of 8°×8°, producing visual experiences that are perceptibly restricted and fail to meet the growing demand for lifelike, wide-angle, three-dimensional displays.

A variety of hybrid or extended SLM schemes have been explored to overcome this angular limitation. These include diffractive optical compensation layers[21–24], artificial phase masks[25,26], random scattering media[27], photon sieves[28,29], and high-numerical-aperture metalenses[30]. While these approaches have incrementally expanded the FOV to 70°×70°[26,31], which is still far below the theoretical full-screen limit. Moreover, they typically entail trade-offs between diffraction efficiency, refresh rate, and image fidelity. Thus, current display architectures reveal a fundamental dichotomy: dynamic control is confined to SLM-based systems, whereas broad angular steering is the hallmark of static metasurfaces. Bridging this divide remains the key to advancing future real-time, full-screen holographic displays.

In this work, we synergistically integrate these two paradigms into a unified platform termed a pixel-interpolation-assisted dynamic holographic meta-projector. Rather than dynamically modulating the metasurface structure itself for static illumination, we propose a conceptually distinct route: employing dynamic structured light illumination, generated by a liquid-crystal SLM, onto a static metasurface engineered with subwavelength precision. This pixel-interpolation strategy effectively merges the microscale pixel modulation of the SLM with the nanoscale scattering control of the metasurface, yielding a composite phase profile that supports both high spatial-frequency manipulation and real-time dynamic operation. Through this cooperative modulation mechanism, the proposed system achieves high-dynamic-range holographic reconstruction, realizing a FOV of 160°×160°—the state-of-the-art performance among dynamic holographic displays to date. Operating at a refresh rate of 60 Hz, well above the temporal resolution limit of human vision, this architecture represents a paradigm shift: it eliminates the need for direct structural reconfiguration of metasurfaces while preserving their intrinsic wide-angle advantage. The demonstrated approach thus establishes a practical and scalable pathway toward real-time, near-full-FOV dynamic holography, with broad implications for immersive visualization, augmented reality, and adaptive optical projection.

Principle of meta-pixel interpolation

Ideal reconfigurable meta-holography realizes dynamic control of light through active metasurfaces (Fig. 1a), which, however, are not achievable nowadays due to poor tunability of nanostructures. Instead, our pixel-interpolation approach achieves dynamic control via a static metasurface combined with spatially structured illumination (Fig. 1b). In this scheme, dynamic holographic reconstruction is enabled by a phase-modulated incident beam generated by a conventional spatial light modulator (SLM). Although the SLM imposes a phase profile with micron-scale pixelation, this pattern is projected onto the underlying static metasurface, where each SLM pixel corresponds to a cluster of distinct subwavelength-phase shifting elements (Fig. 1c). The resulting interpolated phase combines dynamic programmability with effective subwavelength spatial resolution. This in turn enables the generation of high spatial frequencies in the diffracted wavefront, supporting large diffraction angles essential for FOV operation. Consequently, our pixel-interpolation framework not only facilitates the demonstration of large-FOV holographic video but also establishes the physical basis for wide-angle dynamic meta-holography.

Since the dynamic phase comes from only the large-pixel SLM, the interpolated phase is quasi-dynamic, offering a lower degree of tunability than that of an ideal dynamic metasurface hologram. To compensate for this limitation, the metasurface phase profile is pre-optimized to meet specific operational requirements. In this work, for instance, the metasurface is engineered with an expanded phase profile to achieve a record full-screen FOV of 160°×160° (Fig. 1d), as will be experimentally validated in later sections. Consequently, when a sufficiently high-resolution SLM is employed—such as the 2000×2000 pixel device used here—the dynamic SLM phase alone can be tasked with reconstructing arbitrary holographic images.

A pixel-compression process is required prior to pixel interpolation, in which the SLM phase pattern is optically projected onto the metasurface via an imaging system (Fig. 2a). This step is essential for reflective-type SLMs, such as those based on liquid-crystal-on-silicon technology. It also enables effectively zero spatial separation between the SLM and metasurface phase planes. Furthermore, pixel compression reduces the effective SLM pixel size by a scaling factor determined by the imaging optics. Notably, since the entire active area is scaled proportionally, the space-bandwidth product (SBP) of the SLM remains unchanged. This proportional scaling also allows a corresponding reduction in the metasurface dimensions, simplifying its fabrication. We note that pixel compression would be unnecessary if the metasurface could be fabricated at the same scale as the SLM. Figure 2b summarizes the distinct roles of these two operations: pixel compression reduces pixel size and expands the FOV while preserving SBP; pixel interpolation further enhances both SBP and FOV through effective pixel size reduction.

Metasurface phase for FOV expansion

To achieve holographic display with a near-full-screen field of view, we designed a metasurface composed of 6000×6000 unit cells (pitch: 249.3 nm × 249.3 nm) to reconstruct a uniform light field measuring 95.1 mm × 95.1 mm at a distance of z = 8.39 mm (Fig. 3a). Light propagation was simulated using the angular spectrum method, whereby wavevector components are obtained via a two-dimensional fast Fourier transform (FFT) of the incident wavefront—a computationally efficient approach. Under the small-angle approximation, patterns defined in Cartesian coordinates can be directly mapped to k-space. However, at large diffraction angles, these patterns exhibit pronounced distortion in k-space compared to their Cartesian representations.

To visualize this coordinate-mapping distortion, we illustrate four squares of varying angular extents in Cartesian coordinates (Fig. 3b). Following conventional small-angle practice, equivalent squares are plotted directly in k-space (Fig. 3c). When these k-space profiles are rigorously transformed back to Cartesian coordinates (Fig. 3d), the resulting shapes reveal progressively severe pincushion distortion as the FOV increases: at 40°×40°, distortion is minimal; by 90°×90°, the square's corners stretch toward infinity; and at 160°×160°, the shape deviates drastically from a true square.

To address this distortion, we introduce a correction framework in the spatial frequency domain via a parallel point-to-point search algorithm. The coordinates of a point in the xy-plane at a propagation distance z are given by:

$$x = \frac{\alpha\, z}{\sqrt{1-\alpha^{\,2}-\beta^{\,2}}},\; y = \frac{\beta\, z}{\sqrt{1-\alpha^{\,2}-\beta^{\,2}}}, \#\,(1)$$

where α and β are the directional cosines along the x- and y-axes, respectively. A key consideration is the discrepancy between the differential area elements *dxdy* in Cartesian space and *dadβ* in k-space at large diffraction angles. Using the Jacobian determinant in Supplementary Section 6, we derive the transformation

$$dxdy = \left| \frac{\partial\, x}{\partial\, \alpha}\, \frac{\partial\, y}{\partial\, \beta} - \frac{\partial\, x}{\partial\, \beta}\, \frac{\partial\, y}{\partial\, \alpha} \right| d\alpha\, d\beta \;=\; \frac{z^2}{\left(1-\alpha^{\,2}-\beta^{\,2}\right)^2} d\alpha\, d\beta \;=\; \frac{z^2}{\gamma^{\,4}} d\alpha\, d\beta\,, \#\,(2)$$

where $\gamma = \sqrt{1-\alpha^{\,2}-\beta^{\,2}}$ represents the directional cosine along the z-axis. Applying Eq. (1) to transform the Cartesian squares from Fig. 3b into k-space yields the rounded profiles shown in Fig. 3e, where all wavevectors within each square remain bounded by k_0. While Eq. (1) governs the coordinate transformation, Eq. (2) enables brightness correction to account for energy conservation. In k-space, the 160°×160° FOV square exhibits pronounced compression at its corners. To compensate and preserve energy distribution, the intensity in corresponding regions (Fig. 3f) is scaled by γ^{-4}. After this adjustment, the log-scaled intensity attains a maximum value of 4,254 at the four corners, indicating that an equivalent of 4,512 pixels in Cartesian coordinates are compressed into a single pixel in the spatial-frequency domain. Therefore, by formulating an appropriate coordinate transformation and implementing a corresponding brightness correction, we effectively mitigate distortions induced by coordinate mapping at wide angles. This approach facilitates efficient k-space optimization using the fast Fourier transform.

As illustrated in Supplementary Fig. 1a, the phase optimization is performed via gradient descent, initialized with a quadratic phase profile (Supplementary Section 1) to promote uniform initial light dispersion and ensure convergence. The error function is defined as a weighted mean square error between the diffraction pattern intensity and the target distribution in spatial frequency space. In accordance with Eq. 2, a weighting factor of γ^4 is applied at each coordinate to mitigate over-representation of high-spatial-frequency components. As depicted in Fig. 3g, the weighted root-mean-square error (WRMSE) between simulated and target patterns decreases monotonically with iteration count, while diffraction efficiency experiences a slight decline. After 200 iterations, the resulting expansion phase (Fig. 3h) is experimentally realized using titanium dioxide (TiO_2) circular nanopillars (fabrication details in Methods; scanning electron microscopy image in Fig. 3k). By applying two-dimensional interpolation coupled with brightness correction, the k-space diffraction pattern is mapped back to Cartesian coordinates, yielding a relatively uniform distortion-free intensity profile (Fig. 3i).

To further validate the accuracy of the retrieved phase (Fig. 3h), we performe cross-verification using Rayleigh–Sommerfeld diffraction[18,32]. The substantial scale difference between the target image (95.1 mm × 95.1 mm) and the metasurface (1.496 mm × 1.496 mm) precludes the use of FFT-based Rayleigh–Sommerfeld propagation[33] for phase optimization, as it requires identical sampling periods at both planes. This constraint would necessitate an impractical grid size (514,560 × 514,560 samples) at the target plane, exceeding typical computational memory limits. While highly accurate, this method is therefore suitable only for numerical verification, not for iterative optimization.

Simulated intensity distributions across a 160°×160° square region at z = 8.39 mm, obtained via the angular spectrum method (Fig. 3i) and the split-step Rayleigh–Sommerfeld diffraction (Fig. 3j, see its simulation details in Supplementary Section 3), show strong agreement. Slightly enhanced speckling in Fig. 3j stems from the finite diffraction distance in the Rayleigh–Sommerfeld model, unlike the infinite-distance assumption underlying the design in Fig. 3i. Experimentally, the metasurface is illuminated with quasi-collimated light, yielding the directional pattern in Fig. 3l. Slight barrel and pincushion distortions arise primarily from deviations in collimation and angle of incident beam, which bring pronounced aberrations at such extreme FOVs. The central hotspot corresponds to unmodulated transmitted light in metasurfaces. The measured total efficiency of the metasurface approaches 45.1% (Supplementary Section 4), which may be underestimated due to partial collection loss at large diffraction angles.

Retrieval of SLM phase for pixel-interpolation meta-holography

To design the SLM phase, we develop a modified Gerchberg-Saxton algorithm [34] (Fig. 4a) that incorporates data up/down-sampling processes to align with the pixel-interpolation framework of our system. First, the process begins by applying coordinate transformation and brightness correction (Eqs. 1–2) to the target image—here, a "dragon" pattern (Fig. 4b)—mapping it from Cartesian to spatial-frequency (k-space) coordinates. Second, the initial phase φ_0 and incident field A_0 are then up-sampled from an M×M grid to N×N, where M and N denote the pixel counts along one dimension of the SLM and metasurface, respectively. This ensures the incident field and metasurface share the same spatial sampling (N×N). The up-sampled field, superposed with the metasurface phase, undergoes forward propagation via a Fourier transform (FT), yielding an updated phase φ_T for use in the subsequent backward step. Third, Using φ_T together with the pre-compensated target image, we perform inverse propagation (denoted as FT^{-1}) to obtain the phase φ_{inv}, which encodes the target image information. The metasurface phase φ_{META} is then subtracted from φ_{inv} to update the initial SLM phase as φ_{SLM}, completing one iteration. Finally, upon convergence, the final SLM phase φ_{SLM} is obtained by down-sampling the resulting N×N phase distribution back to the original *M×M* SLM resolution (see Supplementary Section 5 for details).

Figure 4c presents the optimized SLM phase after 50 iterations, designed to project a “dragon” pattern (Fig. 4d) measuring 95.1 mm × 95.1 mm at a distance of z = 8.39 mm. Here, a pixel-scaling factor of 3 (i.e., *N/M* = 6000/2000) is applied between the metasurface and the compressed SLM. Experimental

validation was carried out using a custom-built optical setup (schematic in Fig. 4e; full details in Methods). The reconstructed image captured at the screen (Fig. 4f) clearly reproduces the intended “dragon” pattern without significant distortion, confirming the effectiveness of our distortion pre-compensation strategy for a hologram with a FOV of 159.4° × 159.2°. A central bright spot, attributable to unmodulated incident light, is also observed.

To clarify the functional contribution of the metasurface, we performed a control experiment in which the metasurface was removed while all other components remained unchanged. Both simulations (Fig. 4g) and experimental results (Fig. 4h) show that the output degrades into a diffuse bright spot, even when the SLM is programmed with the phase map from Fig. 4c. This outcome underscores that the metasurface is indispensable not only for expanding the FOV but also for enabling meaningful image formation.

We further investigated the impact of misalignment between the compressed SLM phase and the metasurface by introducing controlled lateral shifts (Δx) ranging from 0 to 400 μm. As shown in Fig. 4i, the reconstructed dragon pattern remains discernible but becomes progressively cropped with increasing offset. Notably, the holographic image retains its structural integrity even under substantial displacement and does not vanish, demonstrating a favourable tolerance to misalignment that supports practical implementation. This advantage originates from the regularly distributed phase of metasurfaces so that the lateral misalignment leads to only a small shift of the reconstructed images and will not destroy the image quality severely. In comparison, other methods based on random distributed phase are very sensitive to the misalignment between the SLM phase and the fabricated masks[26,35], thereby increasing the experimental difficulty in achieving the expected images.

Notably, our approach imposes no constraints on the selection of target images—a distinct advantage over conventional dynamic meta-holography systems, which typically support only a limited set of pre-designed patterns. For any given target image, the corresponding SLM phase can be optimized using the algorithm outlined in Fig. 4a. Furthermore, dynamic switching between different images is achieved by simply updating the SLM phase in real time.

Large-FOV meta-holographic images

To illustrate the advantage of our approach over the pixel-compression-only approach, we designed a holographic image with a field of view (FOV) of 160°×160°, approaching the theoretical expansion limit of the fabricated metasurfaces. The experimentally captured result (Fig. 5a) confirms a FOV of ~ 159°×159°, though some nonuniformity is observed due to insufficient sampling in the spatial-frequency domain, suggesting that denser sampling would further improve reconstruction fidelity.

In a control experiment, we removed the metasurface from the optical setup (Fig. 4e), leaving only the pixel-compression architecture. Based on the compressed SLM pixel size (~ 0.748 μm), the theoretical maximum FOV is 44°. However, constrained by the numerical aperture of lens L_4 (focal length: 30 mm,

diameter: 1 inch), the SLM-only hologram was redesigned for half of this maximum FOV. The resulting pattern (Fig. 5b) exhibits a measured FOV of ~ 22.3°×22.3°, see more experimental details in Supplementary Section 7. By comparison, our metasurface-assisted system achieves a FOV enhancement of approximately 7×7 relative to the pixel-compression-only case. This result represents the largest FOV reported to date among dynamic holographic systems[21–25,27,28,30] (see Fig. 1d for comparative analysis), underscoring the critical role of our method in advancing full-screen holographic displays.

Large-FOV meta-holographic movies

To demonstrate the dynamic capabilities of our system, we precomputed SLM phase patterns for each frame of a video sequence and addressed them sequentially via their corresponding frame indices. The field of view (FOV) for all frames was set to 157.5°×157.5° to minimize distortion after pre-compensation. Using the optical setup in Fig. 4e, dynamic holographic video was successfully projected onto the screen. Selected frames from the reconstructed sequence are shown in Fig. 5c, depicting a large “dolphin” swimming across the wide angular range. The full video, recorded continuously, is available as Supplementary Movie 1—to our knowledge, the first holographic video demonstrated with such a high FOV.

The frame rate was characterized by toggling between two distinct holographic frames—one with high intensity and the other with low intensity—at the same screen position (insets, Fig. 5d). A photodetector placed at this location recorded a near-periodic electrical signal (Fig. 5d), where high- and low-amplitude levels correspond to the first and 26th frames, respectively. Over a one-second interval, 30 cycles of high and low signals were observed. Fast Fourier transform (FFT) analysis of the temporal signal confirms a fundamental frequency of 30 Hz (Fig. 5e). Since each cycle comprises two distinct frames, the system operates at a video frame rate of 60 Hz, exceeding the typical temporal resolution threshold of the human eye (~ 24 Hz).

Compared to previously reported dynamic meta-holograms[8,36], our pixel-interpolation approach uniquely combines a near-full-screen FOV, high refresh rate, and support for unlimited image content. We summarize key performance metrics—including frame rate, effective pixel size, and theoretical image capacity—for several dynamic meta-holographic systems in Fig. 5f [8,30,35–40]. The comparison highlights that existing systems typically compromise on at least one of these metrics, whereas our method satisfies all essential requirements for practical holographic display, occupying the optimal region in the parameter space (orange area, Fig. 5f). Therefore, these capabilities make the platform particularly suitable for applications in virtual and augmented reality, where high spatial and temporal performance is critical.

Discussion

The FOV in our dynamic meta-holography system could be further extended by engineering metasurface phases with stronger wavefront-expanding properties. Given the subwavelength architecture of metasurfaces, the theoretical FOV limit approaches 180°×180°. For practical deployment, future efforts should focus on increasing the frame rate and enabling multi-color operation. The present video refresh performance can be significantly improved by adopting high-performance graphics processing units and high-speed data interfaces, especially since the Holoeye GAEA SLM natively supports refresh rates up to 60 Hz. Realizing full-color display will require metasurface redesign to mitigate chromatic aberration, along with utilization of the SLM's multi-color mode for time-sequential channel rendering.

In summary, we have realized a pixel-interpolation-assisted dynamic meta-holography platform that reconstructs arbitrary images with an ultra-wide field of view. Our approach synergistically combines the subwavelength pixelation of metasurfaces with the dynamic programmability of SLMs. To address distortion arising from spatial-frequency coordinate mapping, we introduced a tailored coordinate transformation and brightness compensation framework in *k* space. We further developed a modified Gerchberg–Saxton algorithm incorporating up-sampling and down-sampling operations to implement pixel interpolation. This methodology enables the design of SLM phase patterns that—when optically combined with a metasurface—generate holographic images with exceptionally wide FOVs. Experimentally, we demonstrated a holographic display with a FOV of 157.5°×157.5° at a refresh rate of 60 Hz, thereby advancing the prospects of high-dynamic-range, large-FOV holography for virtual reality and assisted driving systems.

Methods

Numerical simulations. In this work, the angular spectrum method is implemented by using a Fourier transform of the incident field. The outputted field is calculated in the *k*-space that can be expressed approximately in terms of the ratio of the lateral position at the target plane to the propagation distance. Under the condition obeying the sampling theorem, the sampling interval at the target plane can be customized arbitrarily in principle to avoid the aliasing effect.

The verification of the phase designed by the Frourier trasnform is implemented via the Rayleigh-Sommerfeld diffraction[18,32]. After the designed SLM phase is interpolated by the metasurfaces, the resulting phase has the subwavelength pixels. Light from each pixel is considered as an ideal point source that can be described by using an analytical diffraction kernel in Rayleigh-Sommerfeld diffraction. Thus, the diffraction field at the target plane can be taken as a superposition of light from all the pixels that are modulated by the corresponding phase. Because the diffraction kernel and the resulting phase are given, we can calculate the rigorous electric fields at arbitrary positions of the target plane without the sampling issues in the FFT-based approaches. The sampling interval at the target plane can be customized arbitrarily due to the analytical diffraction kernel. However, this weighted-summation approach is quite time-cost to calculate the Rayleigh-Sommerfeld diffraction. Due to the symmetry of the square, only the diffraction pattern in the first quadrant is calculated. In this work, the resulting phase has a sampling amount of 6000×6000 (the sampling interval is 249.3 nm) and its diffraction pattern

located at a propagation distance of z = 8.39 mm is sampled with 252000× 252000 in the first quadrant. It takes 2.7 hours to obtain the first quadrant of the diffraction pattern Fig. 3j in a computer (Intel Core CPU i7-12700 @ 2.1G Hz, RAM 32GB). The simulated result is provided in Fig. 3j, which shows good agreement with the experimental pattern in Fig. 3l. In despite of its accuracy, the summation-based approach is inefficient in optimizing the holographic phase.

Design and fabrications of metasurfaces. To realize the metasurfaces, we use circular-shape TiO_2 nanopillars with varying diameters on a glass (BF33) substrate. To obtain sufficient phase modulation at the operating wavelength of 561 nm, the heights of the nanopillars are fixed at 613 nm. The sketch of a single unit cell with a pitch of 249.3 nm ×249.3 nm is shown in Supplementary Fig. 2a. To simulate optical properties of each nanopillar, the finite-difference time-domain method is used here with a periodic boundary condition along x and y directions and perfect matching layers along the z direction. The simulated transmission and the phase delay of these nanopillars are presented in Supplementary Fig. 2b, which shows a phase modulation of 2π via changing the diameter of the nanopillars while the transmission maintains over 90% for most diameters.

The metasurface was fabricated via a sequence of nanofabrication steps beginning with electron-beam lithography. A TiO_2 film of 613 nm thickness deposited on a substrate was spin-coated with a positive-tone electron-beam resist (AR-P 6200) and soft-baked. Exposure was carried out using a 100 kV electron-beam lithography system (JEOL JBX 6300FS). After development, the sample underwent a post-exposure bake to eliminate residual moisture. A 10 nm chromium hard mask was subsequently deposited by electron-beam evaporation. Lift-off was performed to pattern the mask, followed by etching of the TiO_2 layer. Finally, the remaining chromium was removed using a selective wet etchant.

Experimental setup. Figure 4e sketches the optical setup to characterize the pixel-interpolation-based dynamic meta-holograms. A laser with a wavelength of 561 nm is expanded by using a telescope system composed of two spherical lenses L_1 and L_2 so that the incident beam size can match that of the active region (2000×2000 pixels) of a reflective SLM. After carrying the SLM phase, the light is scaled down by using another telescope system (Lenses L_3 and L_4) to realize pixel-pitch compression from 3.74 μm×3.74 μm (SLM's original pixel pitch) to 0.748 μm×0.748 μm (compressed pixel pitch). Thus, the compressed SLM phase is located at the rear plane of the lens L_4. To interpolate the metasurface phase into the compressed SLM phase, we just put the fabricated metasurfaces at the rear plane of the lens L_4 by using high-precision three-dimensional stages.

Declarations

Competing interests

The authors R.-X. X., Y.-Z. L., X.-P. L., D. Z. and F.-W. S. claim no competing interests. The authors Z.-L. D., F.-J. L., Q.-M. D. and K. H. declare the following competing interests. Z.-L. D., F.-J. L., Q.-M. D. and K. H. have filed two patent application related to this work through Jinan University and the University of

Science and Technology of China. The first patent (Z.-L. D., Q.-M. D., F.-J. L., Z. W., M.-X. H. and K. H., “A metasurface-based dynamic color holographic display method, system, device and medium”, patent No. ZL202410162813.4 (2024)) has been granted. This patent applied by Jinan University and University of Science and Technology of China refers to the design method and physical architecture of metasurface-based SLM for large-FOV dynamic display. The second patent (Z.-L. D., Q.-M. D., Z. W., F.-J. L., M.-X. H. and K. H., “A phase retrieval method for spatial-field-based metasurface-based large-FOV holography”, patent No. ZL202410162953.1 (2024)) has been granted. This patent applied by Jinan University and University of Science and Technology of China refers to the phase retrieval in metasurface-based SLM for large-FOV dynamic display.

Author contributions

K. H. conceived the idea. R.-X. X., F.-J. L., Q.-M. D. and Y.-Z. L. conducted the hologram design. F.-J. L., R.-X. X., Q.-M. D., X.-P. L. and Z.-L. D. designed the metasurfaces. F.-J. L. and D. Z. fabricated the samples. R.-X. X., F.-J. L., Y.-Z. L. and D. Z. built the experimental setup and characterized the samples. R.-X. X., F.-J. L., K. H. and F.-W. S. visualized and analyzed the data. K. H., R.-R. X., F.-J. L., D. Z. and Z.-L. D. wrote the manuscript. K. H., Z.-L. D. and D. Z. supervised the project. All the authors discussed the results.

Acknowledgements

This work is supported by the National Key Research and Development Program of China (2022YFB3607300), the National Natural Science Foundation of China (Grant Nos. 62322512, 62225506, 62422506, 62505308, 12474383 and 12134013), the Fundamental Research Funds for the Central Universities (WK2030000108, WK2030000090), CAS Project for Young Scientists in Basic Research (Grant No.YSBR-049). K. H. thanks the support from the University of Science and Technology of China’s Centre for Micro and Nanoscale Research and Fabrication. D. Z. thanks the China Postdoctoral Science Foundation (2023M743364) and Anhui Natural Science Foundation (2508085QA010). Z.-L. D. thanks the Guangdong Provincial Quantum Science Strategic Initiative (GDZX2406004), the Guangdong Basic and Applied Basic Research Foundation (2022B1515020004), and the Guangzhou Science and Technology Program (2024A03J0465, 2025A04J5776). The numerical calculations were partially performed on the supercomputing system at Hefei Advanced Computing Center and the Supercomputing Center of the University of Science and Technology of China.

References

1. Ee, H.-S. & Agarwal, R. Tunable Metasurface and Flat Optical Zoom Lens on a Stretchable Substrate. *Nano Lett.* **16**, 2818-2823, doi:10.1021/acs.nanolett.6b00618 (2016).
2. Li, S.-Q. *et al.* Phase-only transmissive spatial light modulator based on tunable dielectric metasurface. *Science* **364**, 1087-1090, doi:10.1126/science.aaw6747 (2019).

3. Li, J., Yu, P., Zhang, S. & Liu, N. Electrically-controlled digital metasurface device for light projection displays. *Nature Communications* **11**, 3574, doi:10.1038/s41467-020-17390-3 (2020).
4. Rensberg, J. *et al.* Active optical metasurfaces based on defect-engineered phase-transition materials. *Nano Lett.* **16**, 1050, doi:10.1021/acs.nanolett.5b04122 (2015).
5. Karst, J. *et al.* Electrically switchable metallic polymer nanoantennas. *Science* **374**, 612-616, doi:doi:10.1126/science.abj3433 (2021).
6. Meng, C. *et al.* Dynamic piezoelectric MEMS-based optical metasurfaces. *Sci. Adv.* **7**, eabg5639, doi:doi:10.1126/sciadv.abg5639 (2021).
7. Holsteen, A. L., Cihan, A. F. & Brongersma, M. L. Temporal color mixing and dynamic beam shaping with silicon metasurfaces. *Science* **365**, 257-260, doi:10.1126/science.aax5961 (2019).
8. Wang, Q. *et al.* Optically reconfigurable metasurfaces and photonic devices based on phase change materials. *Nat. Photonics* **10**, 60-65, doi:10.1038/nphoton.2015.247 http://www.nature.com/nphoton/journal/v10/n1/abs/nphoton.2015.247.html#supplementary-information (2016).
9. Wang, Q. *et al.* Reconfigurable phase-change photomask for grayscale photolithography. *Appl. Phys. Lett.* **110** (2017).
10. Lohmann, A. W. & Paris, D. P. Binary Fraunhofer Holograms, Generated by Computer. *Appl. Opt.* **6**, 1739-1748, doi:10.1364/ao.6.001739 (1967).
11. Brown, B. & Lohmann, A. Computer-generated binary holograms. *IBM J. Res. Dev.* **13**, 160-168 (1969).
12. Lee, W. H. Sampled Fourier Transform Hologram Generated by Computer. *Appl. Opt.* **9**, 639-643, doi:10.1364/ao.9.000639 (1970).
13. Maurer, C., Jesacher, A., Bernet, S. & Ritsch-Marte, M. What spatial light modulators can do for optical microscopy. *Laser Photonics Rev.* **5**, 81-101, doi:10.1002/lpor.200900047 (2010).
14. Mok, F., Diep, J., Liu, H.-K. & Psaltis, D. Real-time computer-generated hologram by means of liquid-crystal television spatial light modulator. *Opt. Lett.* **11**, 748-750, doi:10.1364/ol.11.000748 (1986).
15. He, J. *et al.* High-order diffraction for optical superfocusing. *Nat. Commun.* **15**, 7819 (2024).
16. Hahn, J., Kim, H., Lim, Y., Park, G. & Lee, B. Wide viewing angle dynamic holographic stereogram with a curved array of spatial light modulators. *Opt. Express* **16**, 12372-12386, doi:10.1364/OE.16.012372 (2008).
17. Pi, D., Liu, J. & Wang, Y. Review of computer-generated hologram algorithms for color dynamic holographic three-dimensional display. *Light Sci. Appl.* **11**, 231, doi:10.1038/s41377-022-00916-3 (2022).
18. Huang, K. *et al.* Photon-nanosieve for ultrabroadband and large-angle-of-view holograms. *Laser & Photonics Reviews* **11**, 1700025, doi:https://doi.org/10.1002/lpor.201700025 (2017).
19. Yang, D.-K. & Wu, S.-T. *Fundamentals of liquid crystal devices*. (John Wiley & Sons, 2014).

20. Zhao, D., Lian, H., Kang, X. & Huang, K. Hybrid-Layer Data Storage with High-Orthogonality Random Meta-Channels. *Engineering*, doi:https://doi.org/10.1016/j.eng.2024.10.014 (2024).
21. Li, Y.-L. *et al.* Tunable liquid crystal grating based holographic 3D display system with wide viewing angle and large size. *Light Sci. Appl.* **11**, 188, doi:10.1038/s41377-022-00880-y (2022).
22. Wang, D. *et al.* Color liquid crystal grating based color holographic 3D display system with large viewing angle. *Light Sci. Appl.* **13**, 16 (2024).
23. An, J. *et al.* Slim-panel holographic video display. *Nat. Commun.* **11**, 5568, doi:10.1038/s41467-020-19298-4 (2020).
24. Xiong, H. *et al.* 3D Multiview Holographic Display with Wide Field of View Based on Metasurface. *Adv. Opt. Mater.* **13**, 2402504 (2025).
25. Tseng, E. *et al.* Neural étendue expander for ultra-wide-angle high-fidelity holographic display. *Nat. Commun.* **15**, 2907, doi:10.1038/s41467-024-46915-3 (2024).
26. Kuo, G., Waller, L., Ng, R. & Maimone, A. High resolution étendue expansion for holographic displays. *ACM Transactions on Graphics (TOG)* **39**, 66: 61-66: 14 (2020).
27. Yu, H., Lee, K., Park, J. & Park, Y. Ultrahigh-definition dynamic 3D holographic display by active control of volume speckle fields. *Nat. Photonics* **11**, 186-192, doi:10.1038/nphoton.2016.272 (2017).
28. Park, J., Lee, K. & Park, Y. Ultrathin wide-angle large-area digital 3D holographic display using a non-periodic photon sieve. *Nat. Commun.* **10**, 1304, doi:10.1038/s41467-019-09126-9 (2019).
29. Huang, K. *et al.* Ultrahigh-capacity non-periodic photon sieves operating in visible light. *Nat. Commun.* **6**, 7059, doi:10.1038/ncomms8059 (2015).
30. Lu, Y., He, J., Wang, H., Zhao, D. & Huang, K. Metalens-assisted wide-angle dynamic holography for 3D full-color display. *Opt. Lett.* **50**, 7243-7246, doi:10.1364/OL.579703 (2025).
31. Maimone, A., Georgiou, A. & Kollin, J. S. Holographic near-eye displays for virtual and augmented reality. *ACM Trans. Graph.* **36**, Article 85, doi:10.1145/3072959.3073624 (2017).
32. Huang, K. *et al.* Planar Diffractive Lenses: Fundamentals, Functionalities, and Applications. *Adv Mater* **30**, e1704556, doi:10.1002/adma.201704556 (2018).
33. Shen, F. & Wang, A. Fast-Fourier-transform based numerical integration method for the Rayleigh-Sommerfeld diffraction formula. *Appl. Opt.* **45**, 1102-1110, doi:10.1364/AO.45.001102 (2006).
34. Gerchberg, R. W. & Saxton, W. O. A practical algorithm for the determination of the phase from image and diffraction plane pictures. *Optik* **35**, 237-246 (1972).
35. Qu, G. *et al.* Reprogrammable meta-hologram for optical encryption. *Nat. Commun.* **11**, 5484, doi:10.1038/s41467-020-19312-9 (2020).
36. Li, J. *et al.* Addressable metasurfaces for dynamic holography and optical information encryption. *Sci. Adv.* **4**, eaar6768 (2018).
37. Li, X. *et al.* Code division multiplexing inspired dynamic metasurface holography. *Adv. Funct. Mater.* **31**, 2103326 (2021).

38. Naeem, T. *et al.* Dynamic chiral metasurfaces for broadband phase-gradient holographic displays. *Adv. Opt. Mater.* **11**, 2202278 (2023).
39. Gao, H. *et al.* Dynamic 3D meta-holography in visible range with large frame number and high frame rate. *Sci. Adv.* **6**, eaba8595, doi:10.1126/sciadv.aba8595 (2020).
40. Liu, Y. *et al.* Dynamic interactive bitwise meta-holography with ultra-high computational and display frame rates. *Opto-Electronic Advances* **7**, 230108-230101-230108-230111 (2024).

Figures

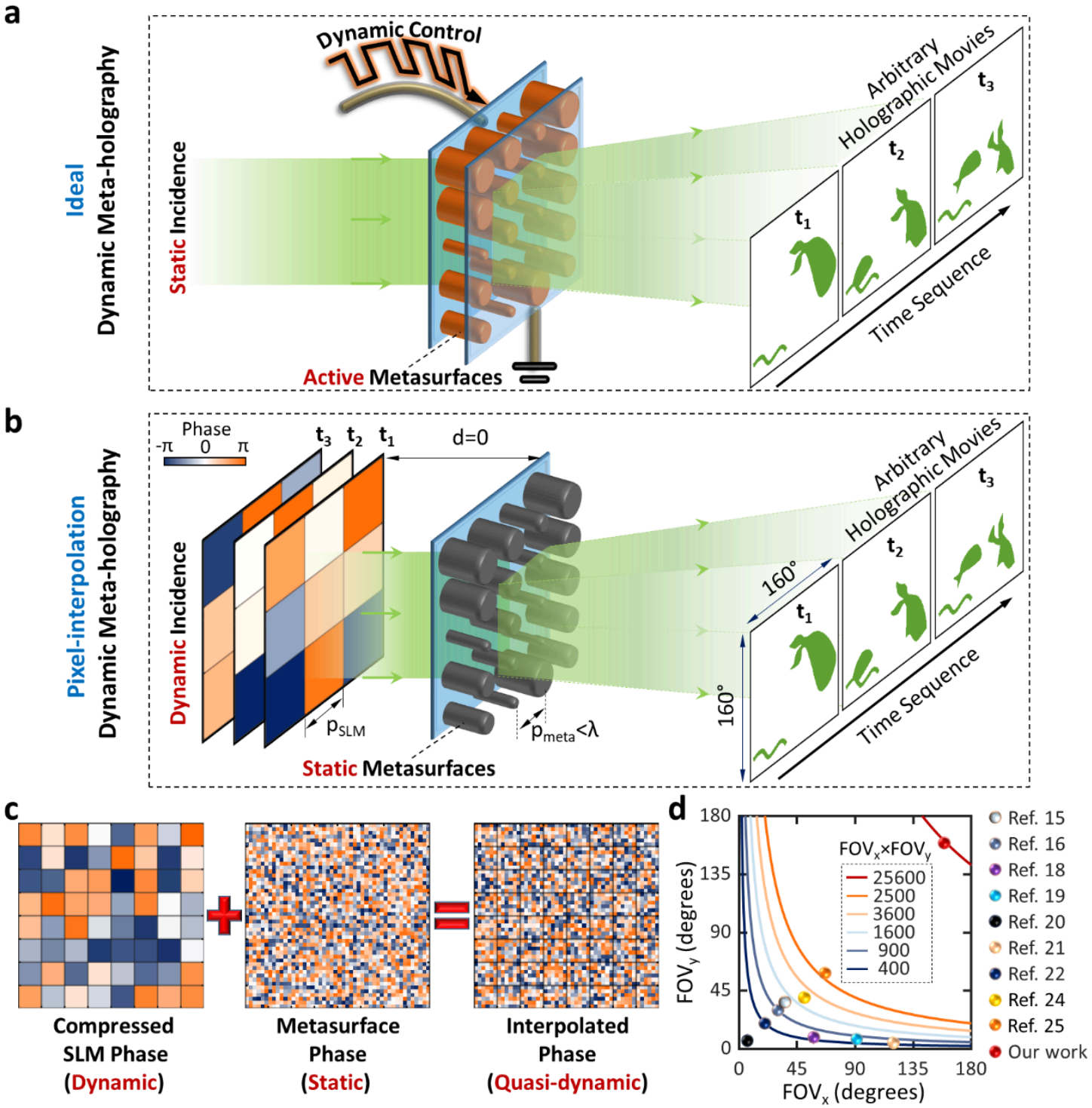


Figure 1

Principle of the pixel-interpolated dynamic meta-holography. **(a)** Ideal dynamic meta-holography by controlling optical properties of each nanostructure actively. It works in a fashion of static incidence and active metasurfaces for dynamic reconstruction of holographic images in a time sequence. However, the challenging active metasurfaces with high reconfigurabilities remain unavailable now. **(b)** Our proposed pixel-interpolated dynamic meta-holography find a new way to employ static metasurfaces and dynamic incidence. The active incidence releases the challenge of realizing active metasurfaces. The static

metasurfaces work as a functionalized device that offers large FOV. It can realize the same functionalities of ideal dynamic meta-holography in reconstructing arbitrary images. **(c)** Sketch for the pixel-interpolation operation in our proposal. The dynamic SLM phase with large pixel pitches is interpolated optically by different metasurface phases with subwavelength pixel pitches. The interpolated phases have both quasi-dynamic and subwavelength pixel pitches for reconfigurable large-FOV holograms. **(d)** A comparison of full-screen FOVs among the reported dynamic holograms for reconstructing arbitrary images. For the works reporting only one-direction FOV[21,22,24], the FOVs along the other direction are extracted from their operating wavelengths and the pixel pitches. It shows the largest full-screen FOV for our proposed dynamic meta-holography.

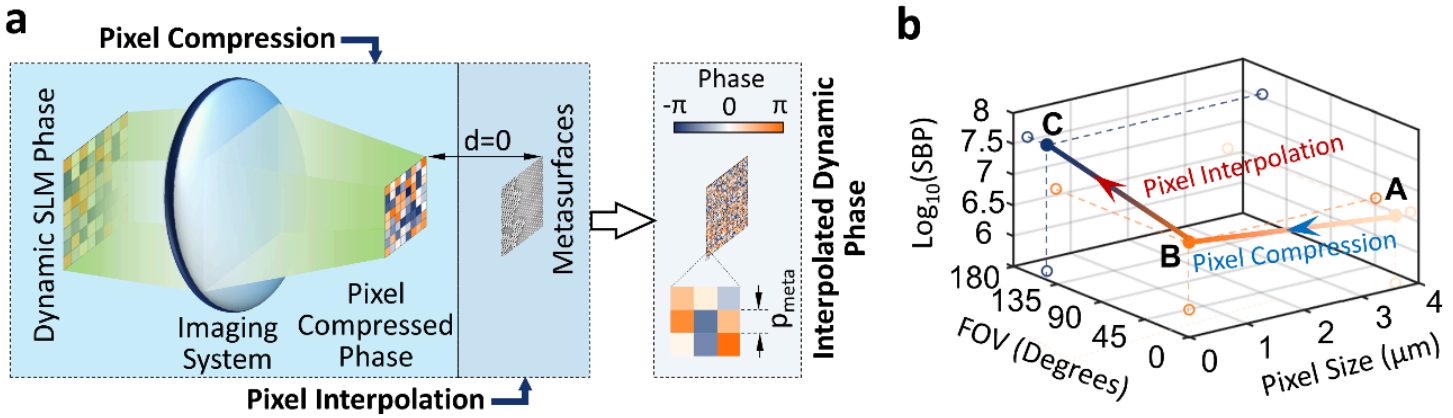


Figure 2

Strategy for practical implementation of the pixel-interpolated dynamic meta-holography. **(a)** Sketch for optical realization of pixel compression and pixel interpolation. The dynamic SLM phase is compressed by an imaging system and projected on the imaging plane. The metasurfaces are located at the imaging plane to realize pixel interpolation optically because the distance between the compressed SLM phase and the metasurface phase can be tuned mechanically to be d=0 in the experiment. **(b)** Spatial-bandwidth product (SBP), FOV and efficient pixel size during the operations of pixel compression and pixel interpolation in the practical pixel-interpolated dynamic meta-holography.

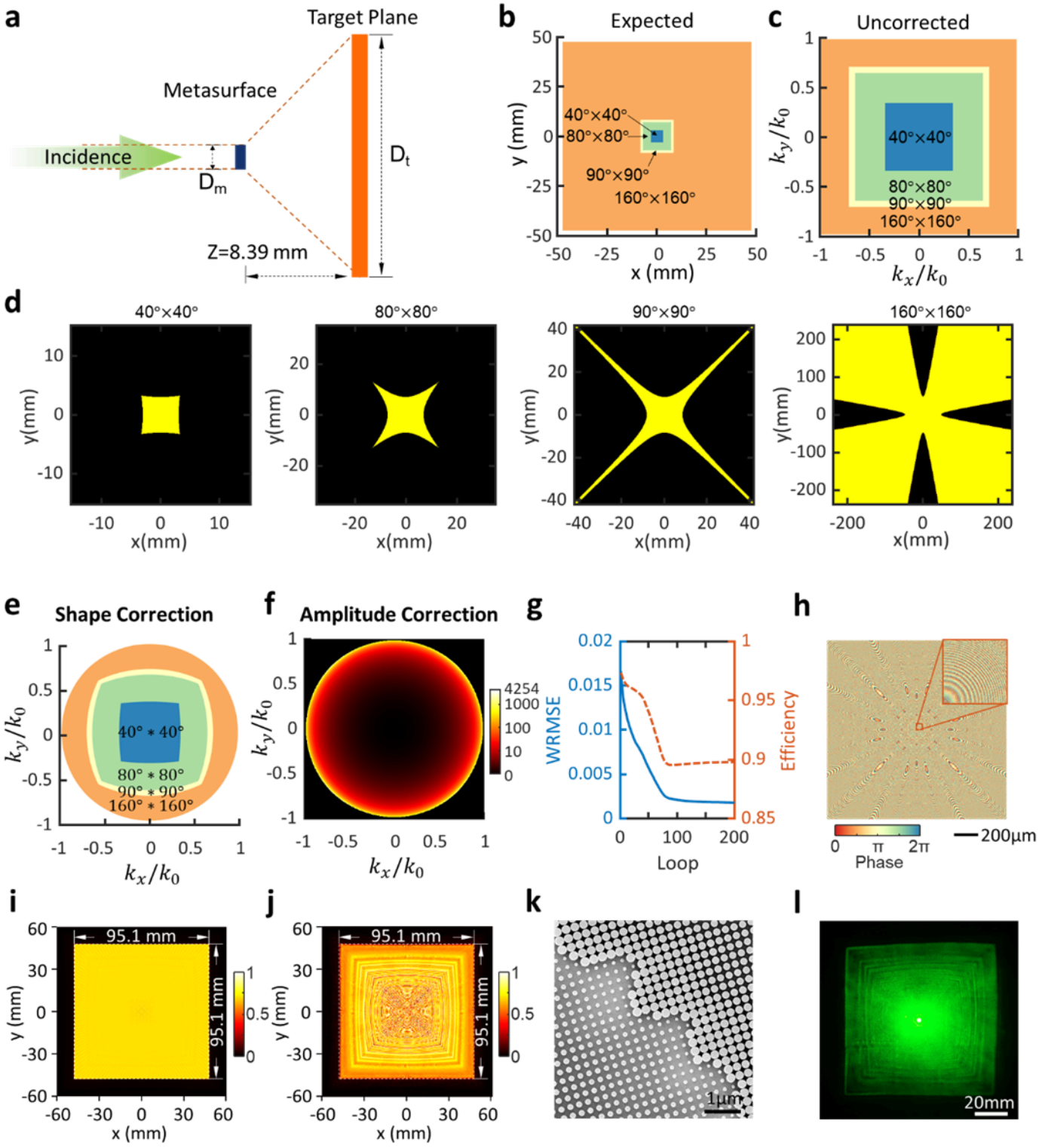


Figure 3

Designing procedure of the FOV expansion metasurface for dynamic hologram. **(a)** Mechanism for designing and characterizing the FOV expansion metasurface. It is implemented by illuminating the metasurfaces (1.496 mm×1.496 mm) with an incident plane wave to generate a uniformly distributed square-shape field (95.1 mm×95.1 mm) with expanded FOV at the propagation distance of z=8.39 mm. The propagation of light is approximated by using the Fraunhofer diffraction. (**b**) Four squares in

Cartesian coordinates with different full FOVs. Four distortion corrected squares in the spatial frequency space with different FOVs. **(e)** Four squares in the *k*-space (**c**) mapped to the Cartesian coordinate system. (**f**) The brightness correction factor of the 160° FOV square, which equals to the fourth power of the spatial cosine γ. **(g)** Weighted root-mean-square error (WRMSE) and diffraction efficiency of the simulated patterns vs the iteration steps (from 0 to 200) of metasurface phase optimization. **(i)**Simulated intensity profile from the designed metasurface phase **(h)** when illuminated by a plane wave. (**j**) Simulated intensity profile from the designed metasurface phase **(h)** by Rayleigh-Sommerfeld diffraction method. (**k**) SEM image (with a titling view) of our fabricated metasurfaces. **(l)** Experimentally captured image at the designed distance of z= 8.39 mm from the metasurface. Because the size of the reconstructed pattern exceeds the effective area of most CCD or CMOS detectors, we used a camera to directly capture the metasurface sample. The hot spot at the center of the sample denotes the unmodulated incident light on the metasurface.

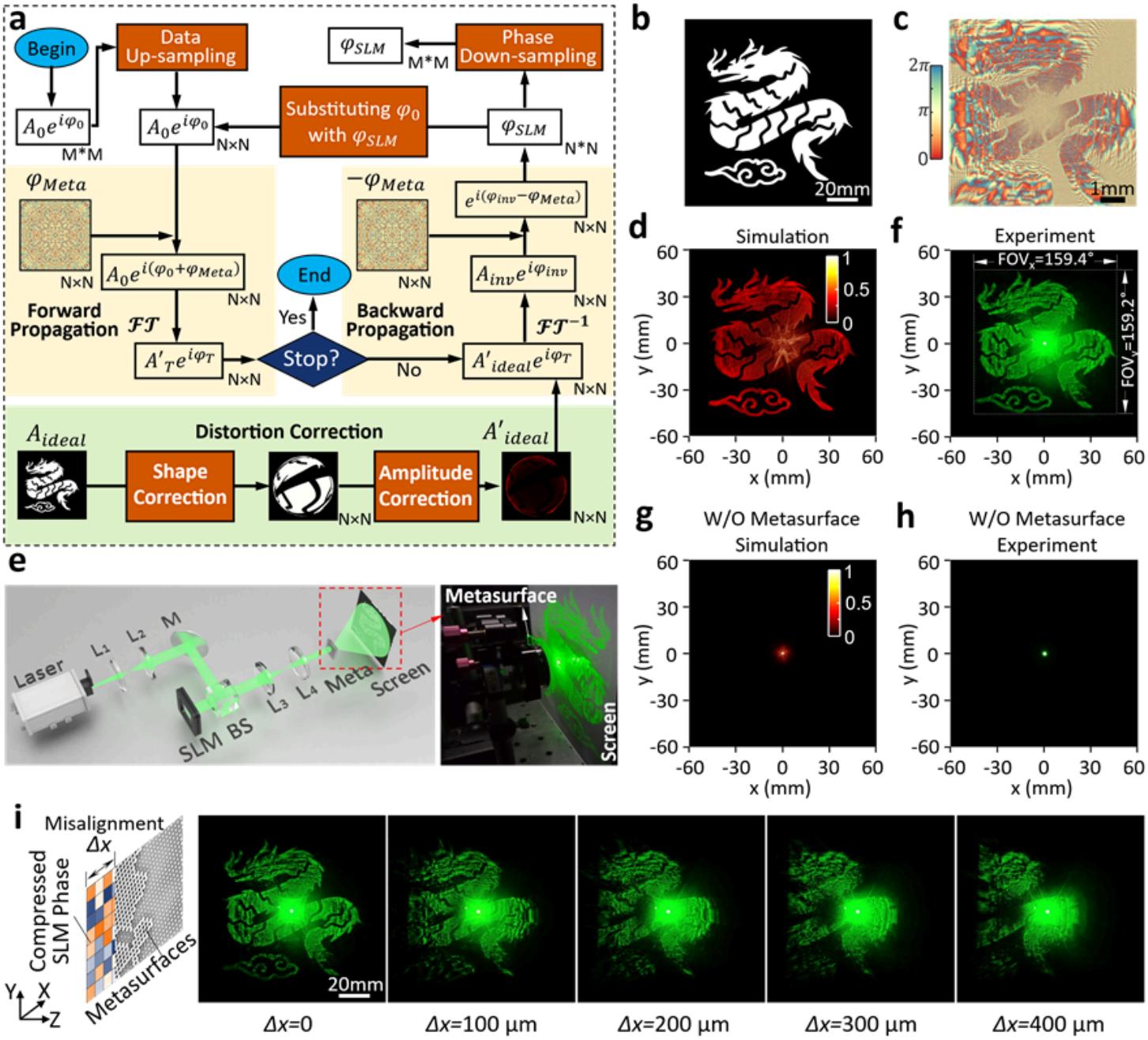


Figure 4

Pixel-interpolation meta-holograms. (a) Flowchart of designing the SLM phase for pixel-interpolation meta-holograms. The up-sampling operation is implemented by dividing one SLM pixel into $(N/M)^2$ metasurface pixels with the same phase, where N is the integer times of M in our proposal. The down-sampling operation is realized by taking one out of every N/M metasurface pixels, thereby making the $N\times N$ metasurface phase profile into a $M\times M$ phase profile for SLM. In this work (N/M=3), each phase at the up-left corner of every 3×3 meta-pixel square is employed to match the $M\times M$ SLM phase. **(b)** Target holographic image with a "dragon" pattern. **(c-d)** Designed SLM phase **(c)** for generating the simulated image **(d)**. In the hologram design, the distortion pre-compensation is used here to avoid the distorted pattern. **(e)** Experimental setup for characterizing the holographic image and the image of the

metasurface diffraction. The inset shows the metasurface device and the screen in holographic display in our laboratory environment. **(f)** Experimentally captured image without obvious distortion. **(g-h)** Simulated **(g)** and experimental **(h)** patterns by removing only the metasurfaces in **(e)**. It is taken as a control experiment to validate the essential role of the metasurfaces in the extremely wide FOV hologram reconstruction.

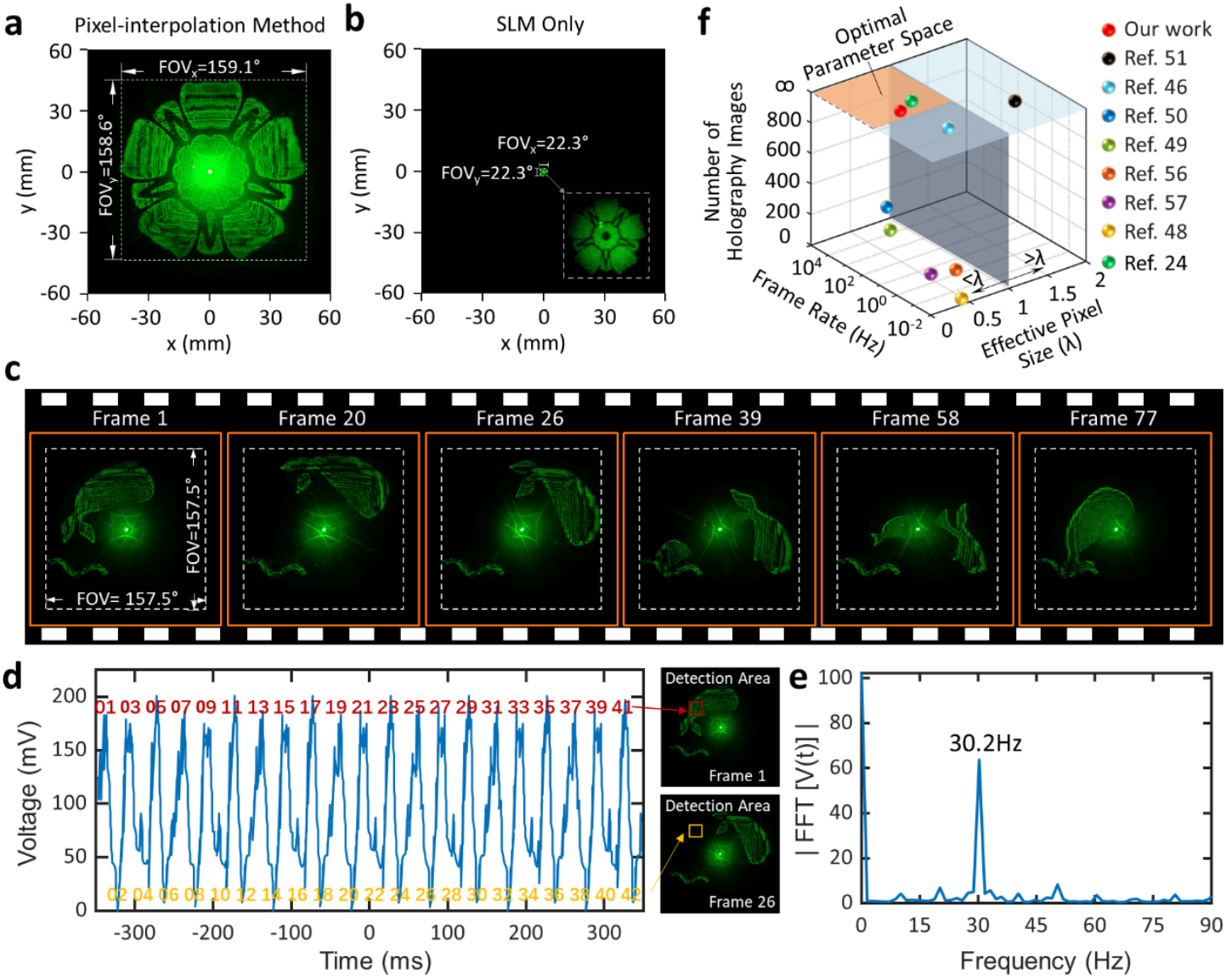


Figure 5

Large-FOV and dynamic features of our pixel-interpolated meta-holography. (a-b) Comparison of experimentally reconstructed images by using our pixel-interpolation method **(a)** and the SLM only **(b)**. It indicates that our method can yield a FOV of 159.1°×158.6° , largely surpass the traditional SLM-only method which create the same pattern with a FOV of 22.3°×22.3°. Figures (**a**) and (**b**) were captured by the camera at the same propagation distance (removing the metasurface slightly affects the actual working distance due to the refractive index of the substrate). A more general comparison of FOVs among different dynamic holograms is provided in Fig. 1d for a better observation. **(c)** Selected frames

in our demonstrated holographic video with a near full-screen FOV of 157.5 °×157.5 °. **(d)** Time-dependent voltage signals of optical detector recording optical fields of two switchable frames. The high and low voltages are relative to the 1^{st} and 26^{th} frames, respectively. **(e)** Fourier transform of the temporal signals in (d) for determining its period, which turns out to be 30. It doubly confirms that 60 frames per second can be achieved in our system. **(f)** Detailed comparison about optical performances (*i.e.*, the largest number of holographic images, effective pixel size and frame rate) of various dynamic meta-holograms. For the holographic display, the optimal parameter space (the orange part) has unlimited image number, subwavelength-scale effective pixel size and high (>24 Hz) frame rate. As the works [8,35,37] that do not provide refreshing rate, we assume that their refreshing rates are 1 for a better comparison.

Supplementary Files

This is a list of supplementary files associated with this preprint. Click to download.

- Supplementary2.51222.docx
- video.mp4